



HAL
open science

Identification of Durable and Non-Durable FeN_x Sites in Fe-N-C Materials for Proton Exchange Membrane Fuel Cells

Jingkun Li, Moulay T Sougrati, Andrea Zitolo, James M Ablett, Ismail Can Oğuz, Tzonka Mineva, Ivana Matanovic, Plamen Atanassov, Andrea Di Cicco, Kavita Kumar, et al.

► **To cite this version:**

Jingkun Li, Moulay T Sougrati, Andrea Zitolo, James M Ablett, Ismail Can Oğuz, et al.. Identification of Durable and Non-Durable FeN_x Sites in Fe-N-C Materials for Proton Exchange Membrane Fuel Cells. 2020. hal-02931434v1

HAL Id: hal-02931434

<https://hal.science/hal-02931434v1>

Preprint submitted on 6 Sep 2020 (v1), last revised 2 Jan 2021 (v2)

HAL is a multi-disciplinary open access archive for the deposit and dissemination of scientific research documents, whether they are published or not. The documents may come from teaching and research institutions in France or abroad, or from public or private research centers.

L'archive ouverte pluridisciplinaire **HAL**, est destinée au dépôt et à la diffusion de documents scientifiques de niveau recherche, publiés ou non, émanant des établissements d'enseignement et de recherche français ou étrangers, des laboratoires publics ou privés.

Identification of durable and non-durable FeN_x sites in Fe-N-C materials for proton exchange membrane fuel cells

Jingkun Li¹, Moulay Tahar Sougrati¹, Andrea Zitolo², James M. Ablett², Ismail Can Oğuz¹, Tzonka Mineva¹, Ivana Matanovic^{3,4}, Plamen Atanassov⁵, Andrea Di Cicco⁶, Kavita Kumar⁷, Laetitia Dubau,⁷ Frédéric Maillard⁷ and Frédéric Jaouen^{1*}

1 Institut Charles Gerhardt Montpellier, UMR 5253, CNRS, Université Montpellier, ENSCM, Place Eugène Bataillon, 34095 Montpellier cedex 5, France

2 Synchrotron SOLEIL, L'orme des Merisiers, BP 48 Saint Aubin, 91192 Gif-sur-Yvette, France

3 The Department of Chemical and Biological Engineering, Center for Micro-Engineered Materials (CMEM), University of New Mexico, Albuquerque, NM 87131, USA.

4 Theoretical Division, Los Alamos National Laboratory, Los Alamos, NM 87545, USA

5 Department of Chemical and Biomolecular Engineering, National Fuel Cell Research Center, University of California Irvine, Irvine, 92697, United States

6 School of Science and Technology, Physics Division, University of Camerino, 62032 Camerino (MC), Italy

7 Univ. Grenoble Alpes, Univ. Savoie Mont Blanc, CNRS, Grenoble INP[‡], LEPMI, 38000 Grenoble, France

[‡] Institute of Engineering Univ. Grenoble Alpes

* To whom correspondence should be addressed.

Email: frederic.jaouen@umontpellier.fr

Abstract

While Fe-N-C materials are a promising alternative to platinum for catalysing oxygen electroreduction in acidic polymer fuel cells, limited understanding of their *operando* degradation restricts rational approaches towards improved durability. Here we show that Fe-N-C catalysts initially comprising two distinct FeN_x sites (S1 and S2) degrade *via* the transformation of S1 into iron oxides while the structure and number of S2 were unmodified. Structure-activity correlations drawn from end-of-test ⁵⁷Fe Mössbauer spectroscopy reveal that both sites initially contribute to the ORR activity but only S2 significantly contributes after 50 h of operation. From *in situ* ⁵⁷Fe Mössbauer spectroscopy in inert gas coupled to calculations of the Mössbauer signature of FeN_x moieties in different electronic states, we identify S1 to be a high-spin FeN₄C₁₂ moiety and S2 a low- or intermediate-spin FeN₄C₁₀ moiety. These insights lay the ground for rational approaches towards Fe-N-C cathodes with improved durability in acidic fuel cells.

Catalysis of oxygen reduction reaction (ORR) is a cornerstone of industrially-relevant electrochemical devices¹ that convert chemical energy into electric power (metal-air batteries,^{2,3} fuel cells (FCs),^{2,4,5}) or electric power into high-added value products (H₂O₂,⁶⁻⁸ Cl₂ with oxygen-depolarized cathodes⁹⁻¹¹). The pH in those devices establishes the ground for selecting materials with promising ORR activity and durability. While proton exchange membrane FCs (PEMFCs) are appealing,¹² their acidic environment is challenging. While platinum-based catalysts now reach high activity and durability,^{13,14} catalysts free of Pt-group-metals remain topical for cost and sustainability reasons. While metal-nitrogen-carbon (M-N-C) catalysts (M=Fe, Co) have demonstrated high ORR activity,¹⁵⁻¹⁸ their durability in PEMFC is poor. Their most active sites are atomically-dispersed MN_x moieties,^{15,16,18} and main degradation mechanisms in acidic medium are i) demetallation,¹⁹⁻²³ ii) surface carbon oxidation *via* Fenton reactions,^{24,25} iii) bulk carbon corrosion,^{21,26,27} iv) protonation of nitrogen groups followed by anion adsorption - a phenomenon particularly important for Fe-N-C catalysts comprising highly basic N-groups.²⁸ Exacerbated demetallation was recently reported in acid for highly-active NH₃-pyrolyzed Fe-N-C catalysts, explaining their poor durability in PEMFC.^{22,29} In contrast, high stability in acidic medium was reported by us for two catalysts exclusively comprising FeN_x moieties, with only 25 % activity decrease after 30,000 load-cycles in Ar-saturated 0.1 M H₂SO₄ at 80°C.²¹ However, after 10,000 load-cycles in the same conditions but in O₂-saturated electrolyte, the decrease in activity and number of FeN_x moieties was 65 and 83 %, respectively, forming iron oxide particles during cycling.³⁰ Therefore, Fe-N-C catalysts comprising more of the durable FeN_x sites and less of the non-durable ones should be targeted. Before the community can engage in this challenge, the identification of which FeN_x sites are durable and which are not is required. It was revealed with *ex situ* ⁵⁷Fe Mössbauer spectroscopy that Fe-N-C catalysts comprise two types of FeN_x sites, labelled D1 (doublet with quadrupole splitting (QS) values of 0.9-1.2 mm·s⁻¹) and D2 (QS=1.8-2.8 mm·s⁻¹)

¹), both having a similar isomer shift (IS).^{15,31,32} By bridging density functional theory calculations on QS-values with *ex situ* Mössbauer spectroscopy, we identified D1 to be a high-spin Fe(III)N_x site (iron site S1) and D2 a low/medium-spin Fe(II)N_x site (iron site S2),³³ in general agreement with two recent studies.^{34,35} While these sites are ubiquitous in Fe-N-C catalysts, their respective activity and durability are unknown.

Here, we separately interrogate S1 and S2 with *in situ, operando* and end-of-test (EoT) spectroscopies (see self-consistent definitions in Supporting Text 1). With *in situ* ⁵⁷Fe Mössbauer spectroscopy in O₂-free PEMFC, we demonstrate that a fraction of S1 is stable, reversibly changing from high-spin ferric to high-spin ferrous state between 0.8 and 0.2 V, while the electronic state of S2 is potential-independent, being ferrous low- or medium-spin. *Ex situ* ⁵⁷Fe Mössbauer spectroscopy at 5 K after PEMFC operation reveals that S2 is durable while S1 is not, with corresponding Fe cations forming ferric oxide nanoparticles. We also provide evidence that S2 is the main contributor to ORR activity in PEMFC after short operation time.

This study was conducted on two Fe-N-C catalysts free of iron clusters, synthesized as previously reported (see Methods)¹⁵ and labelled Fe_{0.5} (pyrolysis in argon) and Fe_{0.5}-950(10) (pyrolysis of Fe_{0.5} in NH₃ at 950 °C for 10 min). Their initial ORR activities in PEMFC (**Figure 1a**) are similar to values reported in Ref.15 and representative for state-of-art Fe-N-C catalysts.^{18,22,36} NH₃ pyrolysis introduces highly-basic nitrogen groups, increasing the turnover frequency (TOF) of FeN_x sites but leading to decreased durability in PEMFC.^{15,17} This was recently explained by higher demetallation rates for NH₃- vs. Ar-treated Fe-N-C catalysts in acid medium,^{17,29} while demetallation rates were equally low in alkaline medium.²⁹ Due to its high stability in acid,²¹ Fe_{0.5} was selected for *in situ* ⁵⁷Fe Mössbauer spectroscopy. The *ex situ*

Mössbauer spectra at 300 K of Fe_{0.5} (powder) and Fe_{0.5}-cathode are identical, identifying only D1 and D2 (**Figure S1a-b**). However, one cannot exclude the formation of superparamagnetic ferric oxides during cathode preparation, which would contribute with a doublet overlapping with D1 signal from S1 sites.³⁷ To unveil this degeneracy, the spectra were acquired at 5 K, a temperature at which nano ferric-oxides contribute with a sextet component,^{38,39} while the signal of S1 remains a doublet.⁴⁰ At 5 K, no sextet was visible for Fe_{0.5} while a sextet representing only 9 % of the absorption area, assigned to ferric oxide, appeared for Fe_{0.5}-cathode (**Figure S1c-d**). Thus, the low-QS doublet in the Fe_{0.5}-cathode spectrum at 300 K can mainly be assigned to S1 sites.

Operando (extended) X-ray absorption near-edge and fine structure (XANES and EXAFS, respectively) was acquired at Fe K-edge in PEMFC (Cell 2,⁴¹ **Figure S2a**, Supporting Text 2). Reversible changes with electrochemical potential were revealed (**Figure 1b**, **Figure S3**), confirming in PEMFC the *in situ* and/or *operando* XANES-EXAFS results previously measured in aqueous acidic electrolyte for Fe_{0.5} and other catalysts comprising only/mostly FeN_x sites.^{2,16,42,43} *Operando* XANES spectra indicate a Fe(III)/Fe(II) redox transition and conformational changes of a significant fraction of FeN_x sites in the region 0.2-0.8 V (**Figure S3a**), while *operando* EXAFS spectra indicate a change from an average O-Fe(III)N₄ to Fe(II)N₄ coordination as the potential is decreased (**Figure S3b**).⁴²⁻⁴⁴ XAS techniques however fail to provide separate information on S1 and S2. To this end, we resorted to *in situ* ⁵⁷Fe Mössbauer spectroscopy with an in-house single-cell PEMFC (Cell 3, **Figure S2b**, Supporting Text 2), whose proper electrochemical response was verified (**Figure S4**). The transmitted γ -ray signal was continuously acquired for 36 h during each *in situ* potentiostatic experiments at room temperature, with humidified H₂/argon at anode/cathode. Following the potentiostatic controls shown in **Figure S5**, we identified irreversible changes in the Mössbauer spectra of

Fe_{0.5}-cathode (during the first two cycles, discussed later) and, thereafter, reversible changes triggered by the potential. **Figure 1c-d** shows reversible changes for *in situ* Mössbauer spectra measured at 0.8 and 0.2 V during cycle 4, labelled 0.8 V (4) and 0.2 V (4). The hyperfine parameters IS and QS of D1 (labelled D1H for *in situ* spectra, see later) and of D2 are similar at 0.8 V (4) to those measured *ex situ* for the pristine Fe_{0.5}-cathode (**Table S1**). In contrast, at 0.2 V (4), both the IS and QS values for D1 (labelled D1L, see later) significantly increased, while those for D2 were unmodified (**Figure 1d**, **Table S1**, row “0.2 V (4)”). After all potential holds (**Figure S5**), we verified with *ex situ* Mössbauer spectroscopy at 5 K that the low-QS doublet (labelled D1H and observed *in situ* at high potential in cycles 1-4) can still be assigned to S1 sites (**Figure S6**). D1H and D1L therefore represent the *in situ* Mössbauer signal of S1 at high and low potential, respectively. **Figure 1c-d** also identifies a third doublet D3, independent of potential and related to irreversible changes occurring to the Fe_{0.5}-cathode during cycle 1 (discussed later).

We now discuss trends for all *in situ* Mössbauer spectra acquired at various potentials. The spectrum 0.8 V (1) shows the doublets D1-D2 (**Figure S7a**), with same IS and QS values than those of the pristine Fe_{0.5}-cathode at 300 K (**Figure S1b**). However, the ratio D1/D2 is lower in 0.8 V (1) (**Table S1**), indicating that some unstable S1 sites were lost during the 36 h-long 0.8 V (1) experiment. From 0.8 V (1) to 0.2 V (1), the spectral parameters and intensity of D2 remained unchanged (**Figure S7a-b**). This applies also to all subsequent potential holds (**Figures S8-S11**). In contrast, the signal from S1 at high potential (D1H) in 0.8 V (1) resulted in a much less intense central doublet in 0.2 V (1) (grey doublet in **Figure S7b**). This indicates demetallation of a significant fraction of sites S1 during the first hold at 0.2 V, in line with 15-40% activity loss after 10k load-cycles in inert gas reported by us for two Fe-N-C catalysts (almost) exclusively comprising FeN_x sites.²¹ Since the 0.2 V (1) spectrum was acquired for

36 h, it may be regarded as a time-averaged spectrum reflecting irreversible phenomena. A detailed analysis of the time-dependence of 0.2 V (1) spectrum clearly reveals this (**Figure S12**, Supporting Text 3). During cycles 2-4 however, the switch between D1H and D1L was triggered solely by the electrochemical potential, with distinct IS and QS values (**Figure 2a-b**, **Figure S8b**). Regarding doublet D3 (IS~1.15·mm s⁻¹ and QS~2.5 mm·s⁻¹), it appeared first in 0.2 V (1) (**Figure S7b**) and is unambiguously assigned to high-spin Fe²⁺ species due to its high IS.^{45,46} The spectral parameters and intensity of D3 remained almost unchanged from 0.2 V (1) and during all subsequent potential holds (**Figure 2e-f**, **Figures S8-S11**). From 0.8 V (2) and afterwards, all spectral changes only reflect the reversible potential dependence of the Mössbauer signature from S1 sites (**Figure 2**, **Figures S8-S10**). To gain understanding on D3, we performed EoT Mössbauer spectroscopy of the Fe_{0.5}-cathode at various temperatures, after completing all *in situ* measurements (**Figure S6b**, **Figure S13-S14**, **Table S2**, Supporting Text 4). In summary, the *in situ* D3 component is assigned to high-spin ferrous oxides, formed from the demetallation of a fraction of S1 sites during 0.2 V (1) (scheme in **Figure S15**). When the EoT Mössbauer spectra are recorded at T ≤ 60 K, such particles contribute with a sextet component assigned to ferric oxide, based on both IS and hyperfine magnetic field (50-56 Tesla).

We now discuss the structures and electronic states of S1 and S2. The *in situ* (absence of O₂) Mössbauer signal of the fraction of S1 sites that survived 0.2 V (1) reversibly switches between D1L at 0.2 V and D1H at 0.8 V (**Figure 2a-b**). D1H is identical to D1 measured *ex situ* on pristine Fe_{0.5}, that we recently identified to be mainly Fe(III)N₄C₁₂ periodic or cluster structures in high-spin state, with axial oxygen adsorbates.^{33,42} Due to its high IS-value, the assignment of D1L to a high-spin Fe(II) species is straightforward.^{45,46} Consequently, only a restricted change in the average iron-spin is expected for Fe_{0.5}-cathode between high and low

potential. We used a three-electrode cell (Cell 4,¹⁶ **Figure S2c**, Supporting Text 2) to verify this with *in situ* Fe K β X-ray emission spectroscopy (XES), a technique well-suited to look into the spin-state of metal centers.⁴⁷ The overlapping *in situ* XES spectra at 0.2 and 0.8 V support that the sites S1 are in high-spin at all potentials (**Figure S16**). The switch from D1H to D1L signal for S1 is thus the outcome of the reduction from Fe(III) to Fe(II), also triggering the removal of an axial OH-adsorbate. To further support this, we applied our recently reported DFT methods³³ to calculate the QS-value of different high-spin OH-Fe(III)N₄C₁₂, OH-Fe(III)N₄C₁₀, Fe(II)N₄C₁₂ and Fe(II)N₄C₁₀ models (**Figure S17**). While high-spin OH-Fe(III)N₄C₁₂ and OH-Fe(III)N₄C₁₀ structures lead to QS-values of 0.6-1.0 mm·s⁻¹, matching those of D1H, only the high-spin Fe(II)N₄C₁₂ structures lead to QS-values of 1.7-2.0 mm·s⁻¹, matching those of D1L (**Table S3**). The QS-values of high-spin Fe(II)N₄C₁₀ structures are >3.0 mm·s⁻¹, significantly higher than those of D1L (**Table S3**). These results confirm our recent assignment of D1 to high-spin Fe(III)N₄C₁₂ structures with axial oxygen ligand,³³ and reveal their switch to high-spin Fe(II)N₄C₁₂ structures, without axial ligand, at low potential (D1L). *Operando* EXAFS spectra (**Figure S3b**) also support that the Fe(III)-to-Fe(II) reduction is accompanied by desorption of oxygen adsorbates.^{42,48} This redox switch is in line with *in situ/operando* XAS on numerous Fe-N-C catalysts^{2,16,42,43} and with the significant presence of S1 in Fe-N-C catalysts.^{15,31,32,42} Here, we show that S1 undergoes this redox transition, but not S2. We then analysed the potential-dependence of the S1 hyperfine parameters. **Figure 3a-b** shows that they can be divided into those below 0.5 V and those above (D1L and D1H, respectively). For comparison, **Figure 3c** reports the DFT-calculated QS for high-spin OH-Fe(III)-N₄C₁₂ and high-spin Fe(II)-N₄C₁₂ structures, demonstrating that our DFT method correctly reproduces the change in QS.

We then attempted to investigate the electronic states and durability of S1 and S2 with *operando* (O_2) Mössbauer spectroscopy. However, this proved impossible for S1. After a single potential hold at 0.2 V in O_2 , no S1 sites were observed in the EoT Mössbauer spectrum at 5 K while two sextets appeared, assigned to ferric oxide particles (**Figure S18a**). The cathode was also characterized with TEM and XRD (**Figure S18b-c**). In contrast, the parameters and absolute intensity of D2 were unmodified before and after 0.2 V hold in O_2 (**Table S4**). This indicates that the electronic state of S2 is potential-independent in the range 0.2-0.9 V and independent on the presence/absence of O_2 . This in turn indicates that S2 is either not accessible to O_2 or binds O_2 weakly, in line with our *ex situ* analysis.³³ The activity of $Fe_{0.5}$ -cathode before and after *operando* measurements (Cell 3) was measured in Cell 1 at 80°C. A restricted ORR-activity decrease from 23 to 15 $mA \cdot cm^{-2}$ is observed at 0.8 V (**Figure S18d**). The remaining activity is much higher than that of the Fe-free N-doped carbon matrix (N-C),¹⁵ implying that either S2 or ferric oxides are active. To evaluate the ORR activity of the latter, we precipitated Fe_2O_3 nanoparticles on the same N-C support. The activity of Fe_2O_3 /N-C above 0.7 V is within reproducibility equal to that of N-C, implying no or negligible ORR activity of Fe_2O_3 (**Figure S19**).

To follow spectral changes as a function of operating time, a series of cathodes was prepared from a same $Fe_{0.5}$ batch and operated at 0.5 V in Cell 1 for either 5, 10, 25 or 50 h. Polarisation curves were recorded before and after each experiment. Each MEA was characterized with EoT ^{57}Fe Mössbauer spectroscopy at 5 K (**Figure 4a-c**, **Figure S20**, **Table S5**). The fittings indicate unmodified spectral parameters and absolute intensity with operation time for D2 with operation time, continuously decreasing signal intensity for D1H and continuously increasing signal intensity for the two sextets, assigned to superparamagnetic ferric oxide (**Figure 4a-c**, **Figure S20**). EoT XANES reveals only minor changes (**Figure S21a**)

while EXAFS spectra after 10-50 h reveal a small increase in the Fe-Fe signal at ~ 2.7 Å, matching the Fe-Fe distance in Fe₂O₃ (**Figure S21b**). X-ray computed tomography performed *ex situ* after 50 h of operation at 0.5 V shows the presence of agglomerated particles (**Figure 4d**, **Figure S22**). The initial and final polarisation curves indicate a sharp activity decrease after 5 h operation at 0.5 V followed by a slow but steady activity decrease (**Figure 4e-f**, **Figure S23**).

To identify structure-activity relationships, we plotted the absolute area of each spectral component and the current density at 0.8 V as a function of time (**Figure 5a-d**). The results indicate a trend of decreased activity with operation time, decreasing amount of sites S1, increasing amount of ferric oxides (sextets) and unchanged amount of sites S2. Based on this, we plotted in **Figure 5e** the current density at 0.8 V as a function of the absolute absorption area for either D1 or (D1+D2). Except for the initial activity measurements, the results reveal a linear correlation between the activity and either D1 or (D1+D2), demonstrating that S1 contributes to ORR activity. The data for the initial activity (star symbol) is an outlier and this can be explained by a higher TOF of Fe-based sites during the first polarisation curve. This hypothesis is in line with our recent work that demonstrated decreased TOF of Fe-based sites by chemical reaction of Fe_{0.5} with H₂O₂.²⁵ The activity drop from 0 to 5 h of operation is thus assigned to both decreased TOF *via* mild surface oxidation of carbon (vertical arrows in **Figure 5e**), and decreased number of S1 sites (arrows along the dashed lines in **Figure 5e**). After 5 h operation, the TOF of the Fe sites seems stabilized, leading to linear correlations between the overall activity and either D1 or D1+D2. The extrapolation at $x = 0$ of the plot of activity *vs.* absolute area of D1 leads however to a positive y-intercept, indicating that the Fe_{0.5}-cathode should have a significant ORR activity even in the absence of S1. This is supported by the results after operation at 0.2 V in O₂ (**Figure S18d**). In contrast, the extrapolation at $x = 0$ of

the plot of activity vs. absolute area of D1H+D2 is near zero, supporting the fact that both S1 and S2 are ORR-active in acidic medium. A rigorous analysis shows that this near-zero y-intercept can be interpreted either as S2 sites being all located on the surface and having a similar TOF as S1, or only a fraction of S2 sites are on the surface and implying then a higher TOF than S1 (Supporting Text 5). We verified that these trends also apply to the initially more active Fe_{0.5}-950(10) catalyst (**Figure S24, Table S6**).

In conclusion, we identify with Mössbauer spectroscopy the high-spin S1 site and the low- or intermediate-spin S2 site, both assigned to FeN₄ moieties but embedded in different ways in the carbon matrix. Iron in the site S1 switches oxidation state III/II in the region 0-1 V while S2 does not, remaining Fe(II). We also identify that both sites initially contribute to the ORR activity of Fe-N-C in acidic medium. However, S1 is not durable in PEMFC, quickly transforming to ferric oxides (**Scheme 1**). In contrast, S2 is shown to be more durable, with no measurable decrease of the number of active sites after 50 h operation at 0.5 V. The lack of change of oxidation state for Fe in S2 in the region 0-1 V is not contradictory with catalysis. For example, we showed with *in situ* XAS that CoN_x sites do not change oxidation state in acidic medium in the same region but catalyze ORR.^{16,44} These results and methods are of high interest to the improved understanding of Fe-N-C materials for application in PEMFC but also in anion-exchange membrane fuel cells and for CO₂ electro-reduction.⁴⁹⁻⁵⁰ For PEMFC application, further efforts should be devoted to increasing the TOF and site density of S2 sites and/or to stabilize S1 in acidic and oxygenated environment. Alternatively, the targeted removal of sites S1 before integrating Fe-N-C materials in PEMFC cathodes would avoid the formation of ferric oxides *in operando*, that likely contribute to peroxide and/or formation of reactive oxygen species.

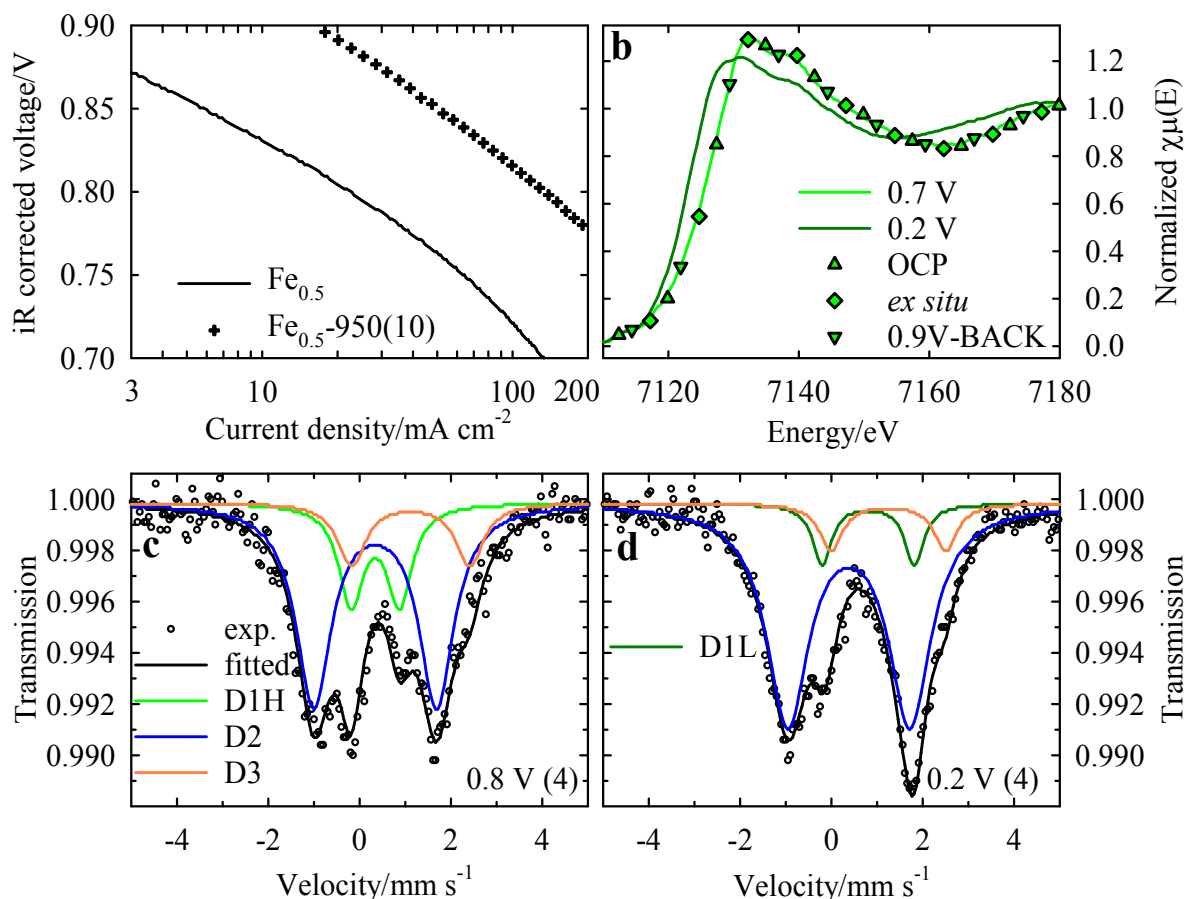


Figure 1. Initial activity of Fe_{0.5}-cathode and reversible spectroscopic changes of the iron centers with potential as observed *operando* or *in situ* in PEMFC. (a) PEMFC Tafel plots of Fe_{0.5} and Fe_{0.5}-950(10); (b) Fe K-edge XANES spectra measured *in situ* in PEMFC as a function of potential; *in situ* ⁵⁷Fe Mössbauer spectra at 0.8 V (c) and 0.2 V (d) acquired during the fourth cycle. For (a), the cell temperature was 80 °C, the flow rates of O₂ and H₂ were 60 sccm with 100% relative humidity, the gauge pressure was 1 bar and the cathode loading was 4 mg·cm⁻². For (b), all the testing conditions were the same as (a), except that no backpressure was applied. For (c-d), the cell was at room temperature, the humidifiers were at 50 °C, Ar and H₂ gases were fed at cathode and anode respectively, and no backpressure was applied. Each Mössbauer spectrum was collected for 36 hours. D1H is the Mössbauer signature of S1 sites at high potential while D1L is their signature at low potential.

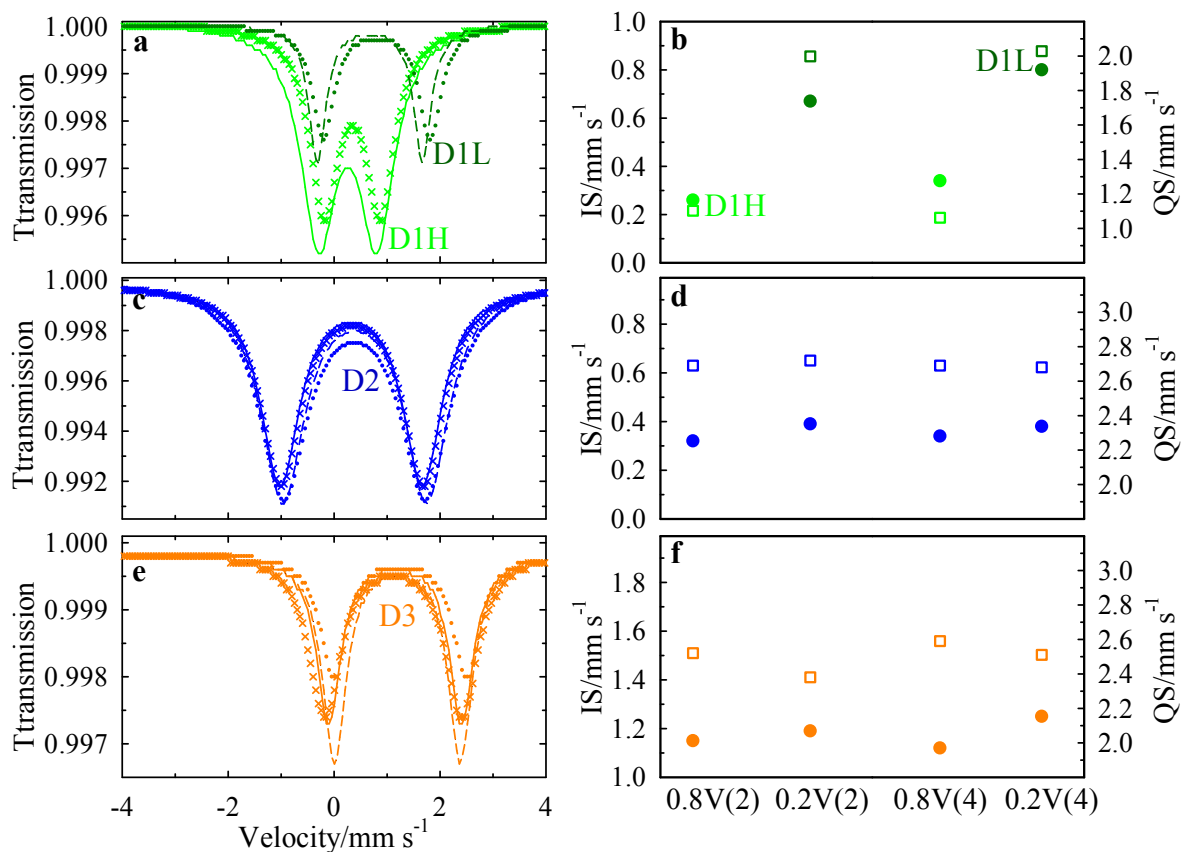


Figure 2. Effect of the electrochemical potential on the spectral components D1, D2 and D3 identified with *in situ* ^{57}Fe Mössbauer spectroscopy in PEMFC. The spectral doublet components D1 (a), D2 (c) and D3 (e) resulting from the fittings, and the corresponding IS and QS values of D1 (b), D2 (d) and D3 (f) at 0.8 V (2), 0.2 V (2), 0.8 V (4) and 0.2 V (4). The number in parentheses represents the cycle number. In (a), (c) and (e), solid curve: 0.8 V (2); dashed curve: 0.2 V (2); \times : 0.8 V (4); \cdot : 0.2 V (4). In (b), (d) and (f), \square : QS; \bullet : IS. D1H is the Mössbauer signature of S1 sites at high potential while D1L is their signature at low potential.

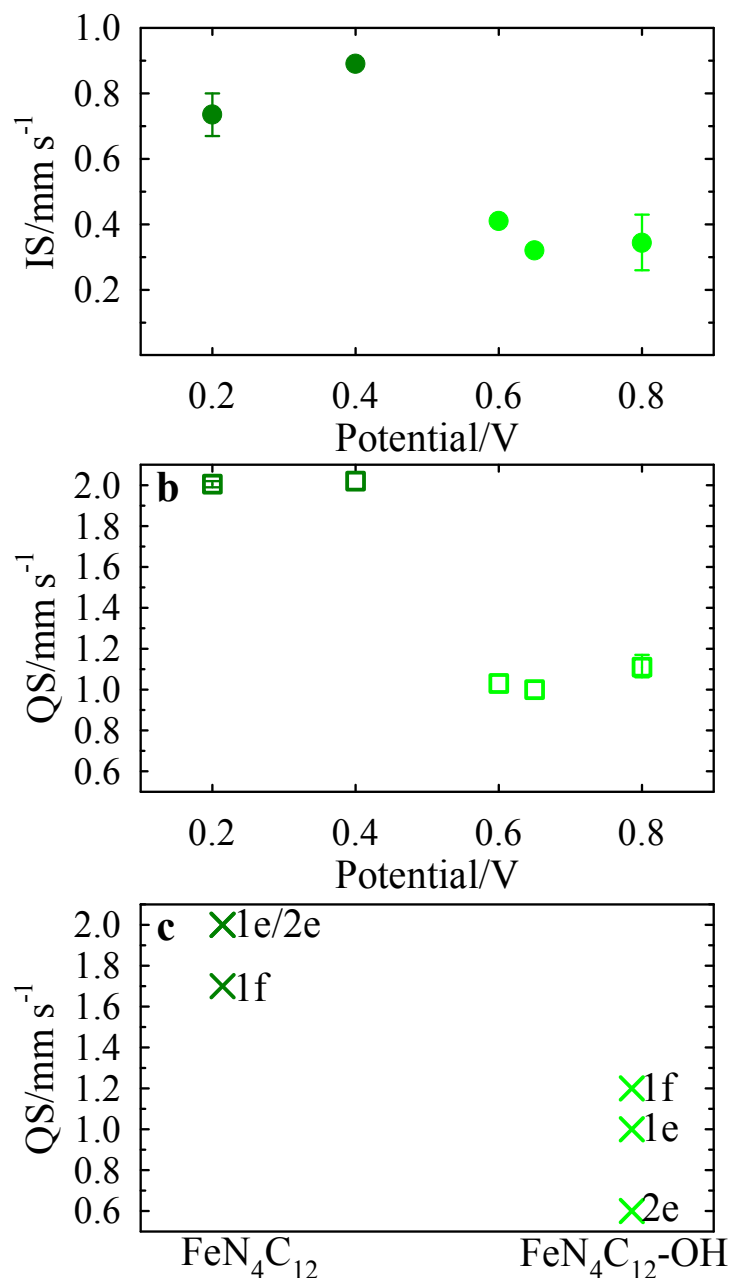


Figure 3. Experimental dependence of the hyperfine parameters IS and QS of the spectral component D1 with electrochemical potential and calculated QS values for high-spin $\text{FeN}_4\text{C}_{12}$ structures. Reversible change of the IS-values (a) and QS-values (b) of the spectral component D1 as a function of the electrochemical potential. (c) The QS-values calculated with PBE/DZVP2 computational method for different $\text{FeN}_4\text{C}_{12}$ model structures in high-spin, with/without oxygen adsorbate. The structures of 1e, 1f and 2e are given in **Figure S17**. QS-values calculated for $\text{FeN}_4\text{C}_{10}$ model structures are given in **Table S3**.

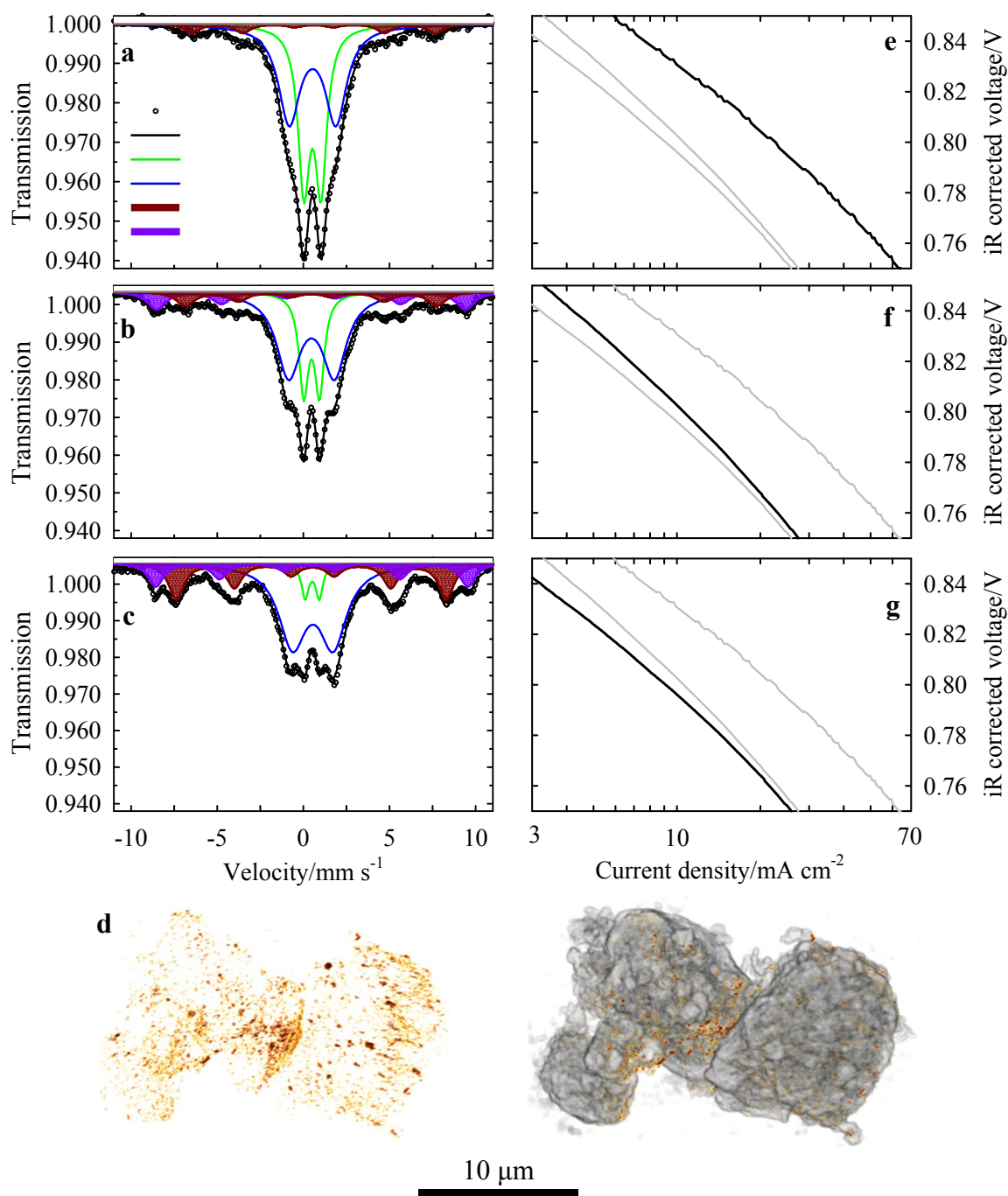


Figure 4. EoT characterisation of $\text{Fe}_{0.5}$ -cathode after durability tests for different duration at 0.5 V in PEMFC. (a) *Ex situ* ^{57}Fe Mössbauer spectrum at 5 K of the pristine $\text{Fe}_{0.5}$ -cathode. EoT Mössbauer spectra at 5 K of the $\text{Fe}_{0.5}$ -cathode after potential hold at 0.5 V in PEMFC for 5 h (b) and 50 h (c). (d) Volume-rendered iron particles (left) and iron particles superimposed onto the morphology of support material (right) of the $\text{Fe}_{0.5}$ -cathode after potential hold at 0.5 V for 50 hours, obtained from X-ray computed tomography with phase

and absorption contrast. The corresponding Tafel plots of Fe_{0.5}-cathode before (e) and after the durability tests for 5 h (f) and 50 h (g). The cell temperature was 80 °C, 60 sccm O₂ and H₂ gases with 100% relative humidity were fed at cathode and anode respectively, the gauge pressure was 1 bar, and the cathode loading was 4 mg·cm⁻².

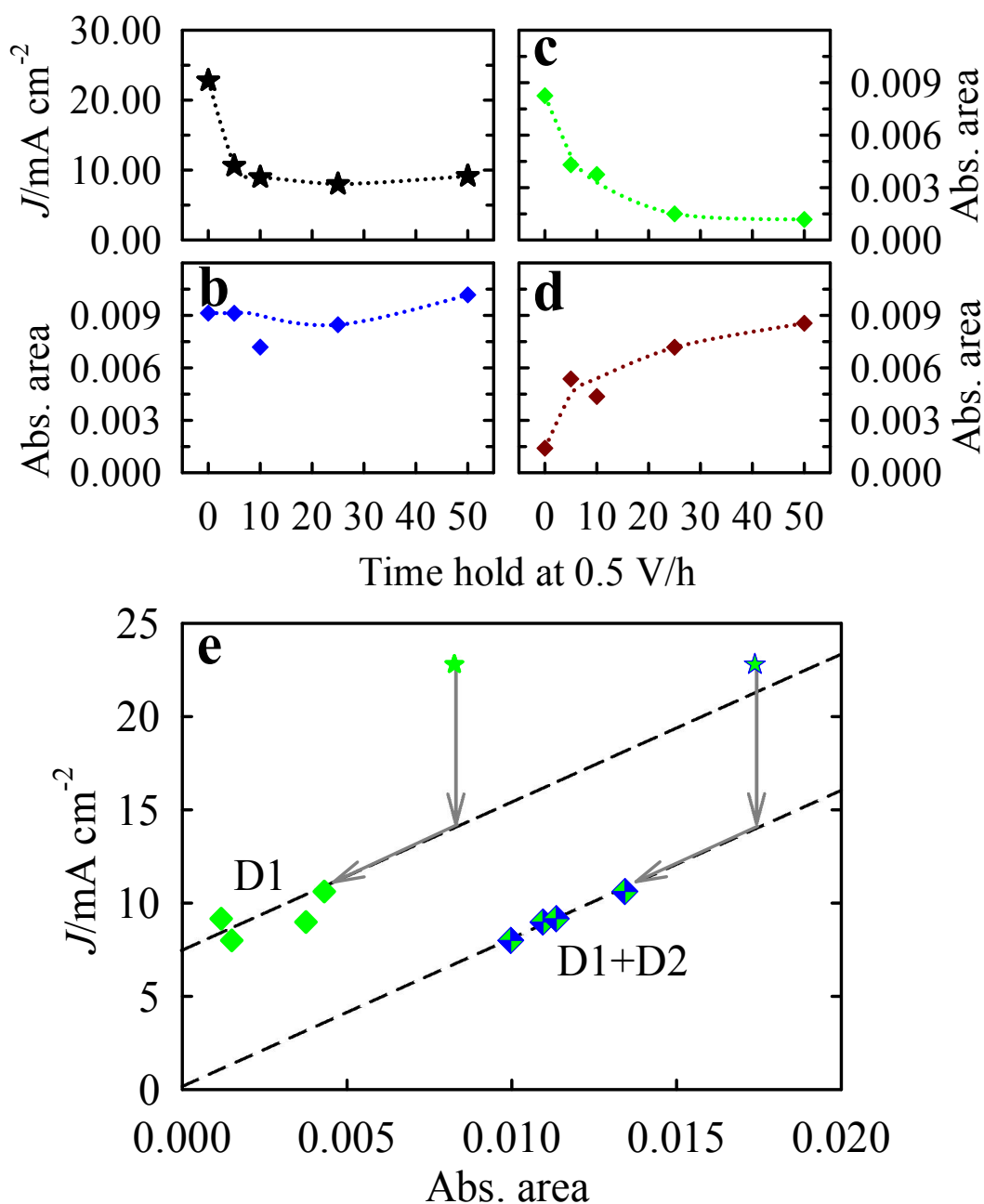
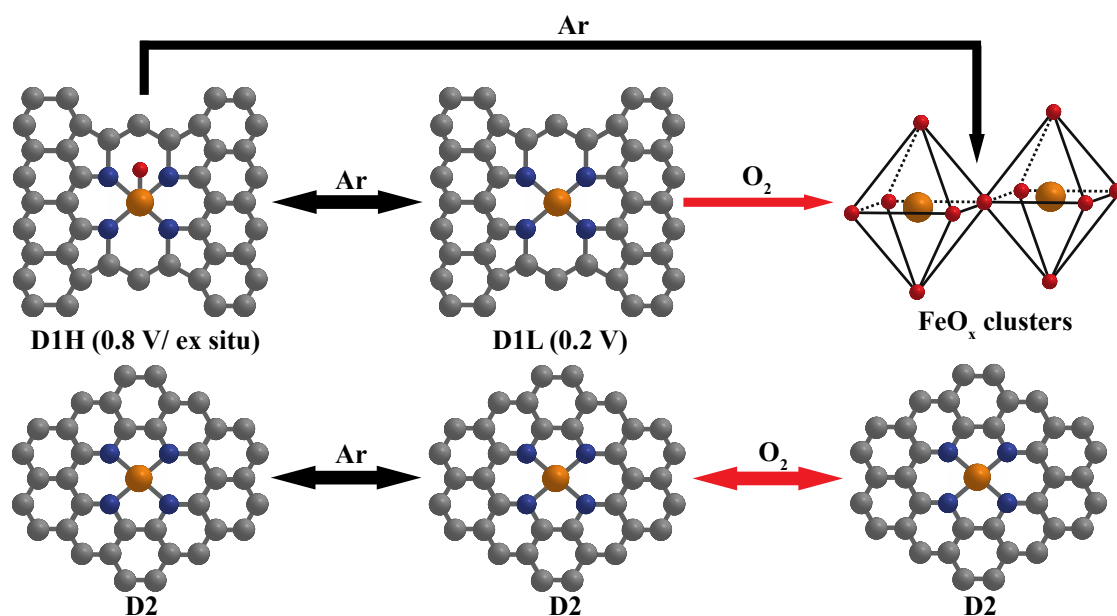


Figure 5. Evolution of the ORR activity and amount of FeN_x sites in the Fe_{0.5}-cathode with operating time at 0.5 V in PEMFC and structure-activity correlations. (a) Current density of the Fe_{0.5}-cathode at 0.8 V vs. duration of operation at 0.5 V in H₂/O₂ PEMFC, absolute absorption areas of D1 (b), D2 (c) and sextets (d) vs. duration of operation at 0.5 V in H₂/O₂ PEMFC. (e) The current density of Fe_{0.5}-cathodes at 0.8 V as a function of the absolute absorption area for D1 and D1+D2. The absolute absorption area of a given spectral component is proportional to the number of corresponding sites in the cathode.



Scheme 1. Coordination or structural changes of the sites S1 and S2 under *in situ* or *operando* conditions. The site S1 is a high-spin $\text{FeN}_4\text{C}_{12}$ structure, undergoing reversible change of Fe oxidation state from III to II *in situ* (no O_2) for the most stable S1-sites fraction (D1H to D1L double-sided black arrow), while the less stable fraction of S1 sites irreversibly transforms *in situ* into ferric oxides (D1H to FeO_x , single-sided black arrow). S1 sites irreversibly transform into ferric oxides *in operando* when catalysing the ORR (single-sided red arrow). S2 sites do not change oxidation state and are stable both *in situ* and *operando* (double-sided arrows).

REFERENCES

1. Katsounaros, I., Cherevko, S., Zeradjanin, A. R. & Mayrhofer, K. J. J. Oxygen electrochemistry as a cornerstone for sustainable energy conversion. *Angew. Chem. Int. Ed.* **53**, 102-121 (2014).
2. Chen, Y., Ji, S., Zhao, S., Chen, W., Dong, J., Cheong, W.-C., Shen, R., Wen, X., Zheng, L., Rykov, A. I., Cai, S., Tang, H., Zhuang, Z., Chen, C., Peng Q., Wang, D. & Li, Y. Enhanced oxygen reduction with single-atomic-site iron catalysts for a zinc-air battery and hydrogen-air fuel cell. *Nat. Commun.* **9**, 5422 (2018).
3. Jung, H.-G., Hassoun, J., Park, J.-B., Sun, Y.-K. & Scrosati, B. An improved high-performance lithium–air battery. *Nat. Chem.* **4**, 579-582 (2012).
4. Sharma, S. & Pollet, B. G. Support materials for PEMFC and DMFC electrocatalysts—a review. *J. Power Sources* **208**, 96-119 (2012).
5. Rahimnejad, M., Adhami, A., Darvari, S., Zirepour, A. & Oh, S.-E. Microbial fuel cell as new technology for bioelectricity generation: a review. *Alex. Eng. J.* **54**, 745-756 (2015).
6. Yin, X., Lin, L., Martinez, U. & Zelenay, P. 2, 2'-Dipyridylamine as Heterogeneous organic molecular electrocatalyst for two-electron oxygen reduction reaction in acid media. *ACS Appl. Energy Mater.* **2**, 7272-7278 (2019).
7. Sun, Y., Silvioli, L., Sahraie, N. R., Ju, W., Li, J., Zitolo, A., Li, S., Bagger, A., Arnarson, L., Wang, X., Moeller, T., Bernsmeier, D., Rossmesl, J., Jaouen, F. & Strasser, P. Activity–selectivity trends in the electrochemical production of hydrogen peroxide over single-site metal–nitrogen–carbon catalysts. *J. Am. Chem. Soc.* **141**, 12372-12381 (2019).
8. Yang, S., Verdaguer-Casadevall, A., Arnarson, L., Silvioli, L., Colic, V., Frydendal, R., Rossmesl, J., Chorkendorff, I. & Stephens, I. E. L. Toward the decentralized electrochemical production of H₂O₂: a focus on the catalysis. *ACS Catal.* **8**, 4064-4081 (2018).
9. Moussallem, I., Pinnow, S., Wagner, N. & Turek, T. Development of high-performance silver-based gas-diffusion electrodes for chlor-alkali electrolysis with oxygen depolarized cathodes. *Chem. Eng. Process.* **52**, 125-131 (2012).
10. Ziegelbauer, J. M., Gullá, A. F., O'Laoire C., Urgeghe, C., Allen, R. J. & Mukerjee, S. Chalcogenide electrocatalysts for oxygen-depolarized aqueous hydrochloric acid electrolysis. *Electrochim. Acta* **52**, 6282-6294 (2007).
11. Li, J., Jia, Q., Ghoshal, S., Liang, W. & Mukerjee, S. Highly active and stable Fe–N–C catalyst for oxygen depolarized cathode applications. *Langmuir* **33**, 9246-9253 (2017).
12. Wang, X. X., Swihart, M. T. & Wu, G. Achievements, challenges and perspectives on cathode catalysts in proton exchange membrane fuel cells for transportation. *Nat. Catal.* **2**, 578-589 (2019).
13. Ott, S., Orfanidi, A., Schmies, H., Anke, B., Nong H. N., Hübner, J., Gernert, U., Gliech, M., Lerch, M. & Strasser P. Ionomer distribution control in porous carbon-supported catalyst layers for high-power and low Pt-loaded proton exchange membrane fuel cells. *Nat. Mater.* (2019) doi:10.1038/s41563-019-0487-0.
14. Huang, X., Zhao, Z., Cao, L., Chen, Y., Zhu, E., Lin, Z., Li, M., Yan, A., Zettl, A., Wang, Y. M., Duan, X., Mueller, T. & Huang, Y. High-performance transition metal–doped Pt₃Ni octahedra for oxygen reduction reaction. *Science* **348**, 1230-1234 (2015).
15. Zitolo, A., Goellner, V., Armel, V., Sougrati, M.-T., Mineva, T., Stievano, L., Fonda, E. & Jaouen, F. Identification of catalytic sites for oxygen reduction in iron-and nitrogen-doped graphene materials. *Nat. Mater.* **14**, 937-942 (2015).
16. Zitolo, A., Ranjbar-Sahraie, N., Mineva, T., Li, J., Jia, Q., Stamatina, S., Harrington, G. F., Lyth, S. M., Krttil, P., Mukerjee, S., Fonda, E. & Jaouen, F. Identification of catalytic sites in cobalt-nitrogen-carbon materials for the oxygen reduction reaction. *Nat. Commun.* **8**, 957 (2017).

17. Proietti, E., Jaouen, F., Lefèvre, M., Larouche, N., Tian, Juan, Herranz, J. & Dodelet, J.-P. Iron-based cathode catalyst with enhanced power density in polymer electrolyte membrane fuel cells. *Nat. Commun.* **2**, 416 (2011).
18. Chung, H. T., Cullen, D. A., Higgins, D., Sneed, B. T., Holby, E. F., More, K. L., Zelenay, P. Direct atomic-level insight into the active sites of a high-performance PGM-free ORR catalyst. *Science* **357**, 479-484 (2017).
19. Choi, C. H., Baldizzone, C., Polymeros, G., Pizzutilo, E., Kasian, O., Schuppert, A. K., Sahraie, N. R., Sougrati, M.-T., Mayrhofer, K. J. J. & Jaouen, F. Minimizing operando demetallation of Fe-NC electrocatalysts in acidic medium. *ACS Catal.* **6**, 3136-3146 (2016).
20. Choi, C. H., Choi, W. S., Kasian, O., Mechler, A. K., Sougrati, M. T., Brüller, S., Strickland, K., Jia, Q., Mukerjee, S., Mayrhofer, K. J. J. & Jaouen, F. Unraveling the nature of sites active toward hydrogen peroxide reduction in Fe□N□C catalysts. *Angew. Chem. Int. Ed.* **56**, 8809-8812 (2017).
21. Kumar, K., Gairola, P., Ranjbar-Sahraie, N., Mermoux, M., Duban, L., Zitolo, A., Jaouen, F. & Maillard, F. Physical and chemical considerations for improving catalytic activity and stability of non-precious-metal oxygen reduction reaction catalysts. *ACS Catal.* **8**, 11264-11276 (2018).
22. Chenitz, R., Kramm, U. I., Lefèvre M., Glibin, V., Zhang, G., Sun, S. & Dodelet, J.-P. A specific demetalation of Fe-N₄ catalytic sites in the micropores of NC_Ar + NH₃ is at the origin of the initial activity loss of the highly active Fe/N/C catalyst used for the reduction of oxygen in PEM fuel cells. *Energy Environ. Sci.* **11**, 365-382 (2018).
23. Ferrandon, M., Wang, X., Kropf, A. J., Myers, D. J., Wu, G., Johnston, C. M. & Zelenary, P. Stability of iron species in heat-treated polyaniline-iron-carbon polymer electrolyte fuel cell cathode catalysts. *Electrochim. Acta* **110**, 282-29 (2013).
24. Lefèvre, M. & Dodelet, J.-P. Fe-based catalysts for the reduction of oxygen in polymer electrolyte membrane fuel cell conditions: determination of the amount of peroxide released during electroreduction and its influence on the stability of the catalysts. *Electrochim. Acta* **48**, 2749-2760 (2003).
25. Choi, C. H., Lim, H.-K., Chung, M. W., Chon, G., Sahraie, N. R., Altin, A., Sougrati, M.-T., Stievano, L., Oh, H. S., Park, E. S., Luo, F., Strasser, P., Dražic, G., Mayrhofer, K. J. J., Kim, H. & Jaouen, F. The achilles' heel of iron-based catalysts during oxygen reduction in an acidic medium. *Energy Environ. Sci.* **11**, 3176-3182 (2018).
26. Choi, C. H., Baldizzone, C., Grote, J.-P., Schuppert, A. K., Jaouen, F. & Mayrhofer, K. J. J. Stability of Fe□N□C catalysts in acidic medium studied by operando spectroscopy. *Angew. Chem. Int. Ed.* **54**, 12753-12757 (2015).
27. Goellner, V., Baldizzone, C., Schuppert, A., Sougrati, M. T., Mayrhofer, K. & Jaouen, F. Degradation of Fe/N/C catalysts upon high polarization in acid medium. *Phys. Chem. Chem. Phys.* **16**, 18454-18462 (2014).
28. Herranz, J., Jaouen, F., Lefèvre, M., Kramm, U. I., Proietti, E., Dodelet, J.-P., Bogdanoff, P., Fiechter, S., Abs-Wurmbach, I., Bertrand, P., Arruda, T. M. & Mukerjee, S. Unveiling N-protonation and anion-binding effects on Fe/N/C catalysts for O₂ reduction in proton-exchange-membrane fuel cells. *J. Phys. Chem. C* **115**, 16087-16097 (2011).
29. Santori, P. G., Speck, F. D., Li, J., Zitolo, A., Jia, Q., Mukerjee, S., Cherevko, S. & Jaouen, F. Effect of Pyrolysis Atmosphere and electrolyte pH on the oxygen reduction activity, stability and spectroscopic signature of FeN_x moieties in Fe-N-C catalysts. *J. Electrochem. Soc.* **166**, F3311-F3320 (2019).
30. Kumar, K., Dubau, L., Mermoux, M., Li, J., Zitolo, A., Nelayah, J., Jaouen, F. & Maillard, F. On the influence of oxygen on the degradation of Fe-N-C catalysts. *Under Review* (Manuscript is attached for review only).

31. Kramm, U. I., Herranz, J., Larouche, N., Arruda, T., Lefèvre, M., Jaouen, F., Bogdanoff, P., Fiechter, S., Abs-Wurmbach, I., Mukerjee, S. & Dodelet, J.-P. Structure of the catalytic sites in Fe/N/C-catalysts for O₂-reduction in PEM fuel cells. *Phys. Chem. Chem. Phys.* **14**, 11673-11688 (2012).
32. Kramm, U. I., Lefèvre, M., Larouche, N., Schmeisser, D. & Dodelet, J.-P. Correlations between mass activity and physicochemical properties of Fe/N/C catalysts for the ORR in PEM fuel cell via ⁵⁷Fe Mossbauer spectroscopy and other techniques. *J. Am. Chem. Soc.* **136**, 978-985 (2014).
33. Mineva, T., Matanovic, I., Atanassov, P., Sougrati, M.-T., Stievano, L., Clémancey, M., Kochem, A., Latour, J.-M. & Jaouen F. Understanding active sites in pyrolyzed Fe-N-C catalysts for fuel cell cathodes by bridging density functional theory calculations and ⁵⁷Fe Mössbauer Spectroscopy. *ACS Catal.* **9**, 9359-9371 (2019).
34. Wagner, S., Auerbach, H., Tait, C. E., Martinaiou, I., Kumar, S. C. N., Kübel, C., Sergeev, I., Wille, H.-C., Behrends, J., Wolny, J. A., Schünemann, V., Kramm, U. I. Elucidating the structural composition of a Fe□N□C catalyst by nuclear and electron resonance techniques. *Angew. Chem. Int. Ed.* **58**, 10486-10492 (2019).
35. Zelenary, P. & Meyers, D. J. Hydrogen and Fuel Cells Program-2019 Annual Merit Review and Peer Evaluation Meeting- ElectroCat (Electrocatalysis Consortium). https://www.hydrogen.energy.gov/pdfs/review19/fc160_myers_zelenay_2019_o.pdf
36. Banham, D., Kishimoto, T., Zhou, Y., Sato, T., Bai, K., Ozaki, J-i, Imashiro, Y. & Ye, S. Critical advancements in achieving high power and stable nonprecious metal catalyst-based MEAs for real-world proton exchange membrane fuel cell applications. *Sci. Adv.* **4**, 7180 (2018).
37. Zboril, R., Mashlan, M. & Petridis, D. Iron(III) oxides from thermal processes - synthesis, structural and magnetic properties, Mössbauer spectroscopy characterization, and applications. *Chem. Mater.* **14**, 969-982 (2002).
38. Kamali-M, S., Ericsson, T. & Wäppling, R. Characterization of iron oxide nanoparticles by Mössbauer spectroscopy. *Thin Solid Films* **515**, 721-723 (2006).
39. Lyubutin, I. S., Starchikov, S. S., Lin, C.-R., Gervits, N. E., Korotkov, N. Y. & Bukreeva, T. V. Structural and magnetic properties of iron oxide nanoparticles in shells of hollow microcapsules designed for biomedical applications. *Croat. Chem. Acta* **88**, 397-403 (2015).
40. Sougrati, M. T., Goellner, V., Schuppert, A. K., Stievano, L. & Jaouen, F. Probing active sites in iron-based catalysts for oxygen electro-reduction: A temperature-dependent ⁵⁷Fe Mössbauer spectroscopy study. *Catal. Today* **262**, 110-120 (2016).
41. Principi, E., Di Cicco, A., Witkowska, A. & Marassi, R. Performance of a fuel cell optimized for *in situ* X-ray absorption experiments. *J. Synchrotron Rad.* **14**, 276-281 (2007).
42. Li, J., Ghoshal, S., Liang, W., Sougrati, M.-T., Jaouen, F., Halevi, B., Mckinney, S., McCool, G., Ma, C., Yuan, X., Ma, Z.-F., Mukerjee, S. & Jia, Q. Structural and mechanistic basis for the high activity of Fe-N-C catalysts toward oxygen reduction. *Energy Environ. Sci.* **9**, 2418-2432 (2016).
43. Osmieri, L., Ahluwalia, R. K., Wang, X., Chung, H. T., Yin, X., Kropf, A. J., Park, J., Cullen, D. A., More, K. L., Zelenary, P., Myers, D. J. & Neyerlin, K. C. Elucidation of Fe-N-C electrocatalyst active site functionality via in-situ X-ray absorption and operando determination of oxygen reduction reaction kinetics in a PEFC. *Appl. Catal. B* **257**, 117929 (2019).
44. Li, J., Alsudairi, A., Ma, Z.-F., Mukerjee, S. & Jia, Q. Asymmetric volcano trend in oxygen reduction activity of Pt and non-Pt catalysts: in situ identification of the site-blocking effect. *J. Am. Chem. Soc.* **139**, 1384-1387 (2017).
45. Fultz, B. "Mössbauer spectrometry." *Characterization of materials* 1-21 (2002).

46. Bonomi, F., Ichiye, T., Hendrich, M., Lindahl, P., Chakrabarti, M., Ribbe, M., Hu, Y., Einsle, O., Jarrett, J., Hille, R. & Booker, S. Characterization, Properties and Applications. Walter de Gruyter GmbH & Co KG. (2017).
47. Vankó, G., Neisius, T., Molnár, G., Renz, F., Kárpáti, S., Shukla, A & de Groot, F. M. F. Probing the 3d spin momentum with X-ray emission spectroscopy: The case of molecular-spin transitions. *J. Phys. Chem. B* **110**, 11647-11653 (2006).
48. Jia, Q., Ramaswamy, N., Hafiz, H., Tylus, U., Strickland, K., Wu, G., Barbiellini, B., Bansil, A., Holby, E. F., Zelenary, P. & Mukerjee, S. Experimental observation of redox-induced Fe–N switching behavior as a determinant role for oxygen reduction activity. *ACS Nano* **9**, 12496-12505 (2015).
49. Hossen, M. M., Artyushkova, K., Atanassov, P. & Serov, A. Synthesis and characterization of high performing Fe-N-C catalyst for oxygen reduction reaction (ORR) in alkaline exchange membrane fuel cells. *J. Power Sources* **375**, 214-221 (2018).
50. Varela, A. S., Kroschel, M., Leonard, N. D., Ju, W., Steinberg, J., Bagger, A., Rossmeisl, J. & Strasser, P. pH Effects on the Selectivity of the Electrocatalytic CO₂ Reduction on Graphene-Embedded Fe–N–C Motifs: Bridging Concepts between Molecular Homogeneous and Solid-State Heterogeneous Catalysis. *ACS Energy Lett.* **3**, 812-817 (2018).

Acknowledgements

The research leading to these results has received partial funding from the French National Research Agency under the CAT2CAT contract (ANR-16-CE05-0007) and the FCH Joint Undertaking (CRESCENDO Project, Grant Agreement n°779366). We acknowledge Synchrotron SOLEIL (Gif-sur Yvette, France) for provision of synchrotron radiation facilities at beamline GALAXIES (proposal number 20170390) and at beamline SAMBA (proposal number 99190122). We sincerely acknowledge Prof. Iryna V. Zenyuk and Ying Huang for X-ray tomography imaging and analysis, under resources of the Advanced Photon Source, a U.S. Department of Energy (DOE) Office of Science User Facility operated for the U.S. DOE Office of Science by Argonne National Laboratory under Contract No. DE-AC02-06CH11357. I. M. thankfully acknowledges the computational resources of the National Energy Research Scientific Computing Center (NERSC), a U.S. Department of Energy Office of Science User Facility operated under Contract No. DE-AC02-05CH11231. This paper has been assigned LA-UR-19-31453. The computational work of T.M and I.C.O. was granted access to the HPC resources of IDRIS/TGCC under the allocation 2019 - A0050807369 made by GENCI and supported by the Labex ChemISyst ANR-10-LABX-05-01.

Author contributions

J.L. and F.J. designed and synthesized the materials, and conducted the electrochemical and physical characterizations. M.T.S. and J.L. designed and conducted the *in situ* and *ex situ* Mössbauer spectroscopy measurements. M.T.S. conducted Mössbauer data analysis. A.Z. and J.L. conducted the *operando* and *ex situ* XAS measurements. A.D.C. designed the *operando* fuel cell for XAS. F.J., A.Z., J.L. and J.M.A. conducted the *in situ* XES experiments. I.C.O., T.M., I.M. and P.A. conducted the DFT computation. K.K., L.D. and F.M. performed the TEM

analysis. J.L., M.T.S. and F.J. wrote and edited the manuscript with input from all authors. The project was supervised by F.J.

Methods

Synthesis. The synthesis of $\text{Fe}_{0.5}$ and $\text{Fe}_{0.5-950(10)}$ was reported previously.¹⁵ Catalyst precursors were prepared from a Zn(II) zeolitic imidazolate framework (Basolite Z1200 from BASF, labelled ZIF-8), Fe(II) acetate (Fe(II)Ac), and 1,10-phenanthroline (Phen). $^{57}\text{Fe(II)Ac}$ was used as iron precursor for all Mössbauer studies. For *operando* XAS, natural Fe(II)Ac was used. The catalyst $\text{Fe}_{0.5}$ was synthesized via the dry ball-milling of ZIF-8 (800 mg), Phen (200 mg) and Fe(II)Ac (16 mg) in a zirconium oxide crucible filled with 100 zirconium oxide balls (5 mm diameter) at 400 rpm for 2 hours (Fritsch Pulverisette 7 Premium, Fritsch, Idar-Oberstein, Germany). The subscript in $\text{Fe}_{0.5}$ corresponds to the Fe content (wt %) in the entire catalyst precursor before pyrolysis. Then the mixed precursor was pyrolyzed in flash mode in Ar at 1050 °C for 1 hour. Owing to a mass loss of 65–70 wt % during pyrolysis in Ar, caused by volatile products formed from ZIF-8 and Phen, the iron content in $\text{Fe}_{0.5}$ is about three times the iron content in the catalyst precursor. $\text{Fe}_{0.5}$ was subjected to a second flash pyrolysis for 10 min at 950 °C in NH_3 , yielding $\text{Fe}_{0.5-950(10)}$. The mass loss of carbon during NH_3 pyrolysis was 25–31%, further increasing the iron content.

The synthesis of $\text{Fe}_2\text{O}_3/\text{N-C}$: First, the Fe-free N-C was synthesized identically with $\text{Fe}_{0.5-950}$ except for the first ball-milling step, where no Fe(II)Ac was added. Then 15 mg of $\text{FeCl}_2 \cdot 4\text{H}_2\text{O}$ was dissolved in 7.5 mL H_2O /ethanol solution (v:v=24:1). Then 300 mg N-C was added, and well-mixed *via* sonication for 1 hour. The obtained slurry was stirred continuously for another 48 hours, followed by filtration, washing with water, and dry in the oven at ~50 °C overnight. The $\text{Fe}_2\text{O}_3/\text{N-C}$ sample was obtained by a final heat treatment at 200 °C for 2 hours in Ar with

a ramping rate of $5\text{ }^{\circ}\text{C}\cdot\text{min}^{-1}$. The Fe content in $\text{Fe}_2\text{O}_3/\text{N-C}$ was found to be 1.3 wt.% by X-ray fluorescence (XRF) spectroscopy.

XRF. The metal content in $\text{Fe}_2\text{O}_3/\text{N-C}$ was measured *via* X-ray XRF spectroscopy (Axios Max from PANalytical, Netherlands). $\text{Fe}_2\text{O}_3/\text{N-C}$ powder was mixed with boric acid as a binder in a ratio of 1:3 by weight *via* ball-milling at 400 rpm for 30 min. Then 200 mg of the mixture was pelletized as a disk of 13 mm diameter for XRF measurements. The calibration curve was performed using 0.1, 0.2, 0.5, 1.0, 1.5 and 2.0 wt% Fe in a mixture of Fe(II)Ac and Vulcan XC72R. The Vulcan XC72R (mixed with Fe(II)Ac) were mixed with boric acid in a ratio of 1:3 by weight *via* ball-milling at 400 rpm for 30 min, and then 200 mg of the mixture was pelletized as a disk of 13 mm diameter.

XRD. X-ray diffraction patterns were recorded using a PANalytical X'Pert Pro powder X-ray diffractometer with $\text{Cu K}\alpha$ radiation.

TEM. A JEOL 2010 Transmission Electron Microscopy operated at 200 kV was used to examine Fe-N-C cathodes before testing or at EoT. The resolution was 0.19 nm.

Electrochemical characterisation. The ORR activities of $\text{Fe}_{0.5}$ and $\text{Fe}_{0.5-950}$ were investigated in a single-cell PEMFC (Cell 1, see also Supporting Text 2). For the membrane electrode assembly (MEA), cathode inks were prepared by sonicating for 1 hour the mixture of 20 mg of catalyst, 652 μL of a 5 wt% Nafion solution containing 15–20% water, 326 μL of ethanol and 272 μL of de-ionized water. Then, three aliquots of 405 μL of the catalyst ink were successively deposited on the microporous layer of a 4.84 cm^2 gas diffusion layer (Sigracet S10-BC). The cathode was then placed at $60\text{ }^{\circ}\text{C}$ to dry for 2 hours. The anode used for all PEMFC tests in Cell 1 was $0.5\text{ mg}_{\text{Pt}}\cdot\text{cm}^{-2}$ on Sigracet S24-BC. Nafion NRE-211 was used as membrane. No hot-pressing was applied in order to easily peel off the cathode for EoT characterisation. PEMFC tests were performed with a single-cell fuel cell with serpentine flow field (Fuel Cell Technologies) using an in-house test bench and a Biologic potentiostat with a

50 A load and EC-Lab software. The fuel cell temperature was 80 °C, the humidifiers were set at 85 °C and the inlet pressures were set to 1 bar gauge for both anode and cathode sides. The flow rate for humidified H₂ and O₂ gases was 60 sccm downstream. No break-in was applied before recording the first polarisation curve. Polarization curves were recorded by scanning the voltage at 1 mV·s⁻¹.

Ex situ and operando XAS. Fe K-edge X-ray absorption spectra were collected at room temperature at SAMBA beamline (Synchrotron SOLEIL). The beamline is equipped with a sagittally focusing Si 220 monochromator, and X-ray harmonics are removed by two Pd-coated mirrors. For *ex situ* measurements on pristine Fe-N-C catalysts, the powders were pelletized as disks of 10 mm diameter with 1 mm thickness, using Teflon powder (1 µm particle size) as a binder and XAS measured in transmission mode. For *ex situ* measurements on Fe-N-C cathodes (before testing or at EoT), XAS was acquired in fluorescence mode. For *operando* XAS experiments, MEAs were prepared identically as for measurements in the commercial PEMFC (Cell 1). The design of the PEMFC used for *operando* XAS study (Cell 2, see also Supporting Text 2) was reported in Ref. 41. The cell temperature was 80 °C, 60 sccm O₂ and H₂ with 100% relative humidity were fed at cathode and anode respectively, and the cathode loading was 4 mg·cm⁻². No backpressure was applied. *Operando* measurements were performed by recording the Kα X-ray fluorescence of Fe with a Canberra 35-elements monolithic planar Ge pixel array detector.

Ex situ and in situ Mössbauer spectroscopy. ⁵⁷Fe-enriched Fe(II)Ac was used as iron precursor for all Mössbauer studies. The ⁵⁷Fe Mössbauer spectrometer (Wissel, Germany) was operated in transmission mode with a ⁵⁷Co: Rh source. The velocity driver was operated in constant acceleration mode with a triangular velocity waveform. The velocity scale was calibrated with the magnetically split sextet of a high-purity α-Fe foil at room temperature. The spectra were fitted to appropriate combinations of Lorentzian profiles representing quadrupole

doublets, sextets by least-squares methods. IS values are reported relative to α -Fe at room temperature. For *ex situ* measurements on pristine Fe-N-C catalysts, powders (20-30 mg) were mounted in a 2 cm² holder. For *ex situ* measurements on Fe-N-C cathodes, before testing or at EoT, 5 cm² electrodes were cut into four pieces and stacked on each other. Mössbauer measurements below 100 K were performed in a helium flow cryostat (SHI-850 Series from Janis, USA). For *in situ* Mössbauer experiments, MEAs were prepared as described for testing in the commercial PEMFC (Cell 1), except that the anode was 0.1 mg_{Pt} cm⁻² to maximize γ -ray transmission through the cell. The design of the PEMFC for *in situ* Mössbauer spectroscopy (Cell 3, see also Supporting Text 2) is shown in **Figure S2b**. The cell was at room temperature, the humidifiers were at 50 °C, Ar and H₂ gases were fed at cathode and anode respectively, and no backpressure was applied. The Mössbauer signal was continuously acquired for 36 hours at each cathode potential.

***In situ* XES.** Fe K _{β} X-ray emission spectra were collected at room temperature using a 1m radius Germanium 620 analyzer crystal at GALAXY inelastic scattering end-station (Synchrotron SOLEIL).⁵¹⁻⁵² The incident energy was 8500 eV (using a silicon double-crystal monochromator) and the focused beam size was 30 [ver.] x 90 [hor.] μ m². The sample, analyser crystal and silicon drift detector were all arranged in a vertical Rowland circle geometry and air absorption was reduced by using helium flight paths. The electrochemical cell (Goodfellow cat. C 000200/2) used for *operando* XES in liquid electrolyte with a three electrode system is the same as the one previously for *in situ* or *operando* XAS measurements (Cell 4, see also Supporting Text 2).¹⁶ Catalyst inks were prepared by mixing 10 mg catalyst with 50 μ L de-ionized water and 100 μ L of 5 wt% Nafion® solution with ultrasounds. A 50 μ L aliquot was then pipetted on \sim 3 cm² circular area of a 100- μ m-thick graphite foil, resulting in a catalyst loading of \sim 1 mg \cdot cm⁻². The graphite foil with deposited catalyst then served as a working electrode, Ag/AgCl and Pt were used as reference and counter electrodes, respectively.

The cell was filled with 0.5 M H₂SO₄ and saturated with N₂ by continuously bubbling gas in the electrolyte.

X-ray computed tomography (CT). X-ray CT imaging was performed at the Advanced Photon Sources (APS) at Argonne National Laboratory (ANL) using Beamline 32-ID. Fresnel zone plates with grading of 60 nm were used to achieve resolution of 60 nm. Zernike phase contrast was used to detect soft elements, whereas absorption contrast was used for imaging hard materials. Image phase retrieval and reconstructions were performed using TomoPy.

DFT computation. Density functional theory (DFT) spin-polarized calculations were carried out with the cluster and periodic approaches using respectively, deMon2k.6.0.2 developers version^{53,54} and VASP^{55,56} computer programs on graphene sheets (with defects) integrating various moieties from the ferrous and ferric FeN₄C₁₀ and FeN₄C₁₂ sub-groups. The considered cluster and periodic models are reported in **Figure S17**. The dangling bonds in all structures were saturated with hydrogen atoms. In the cluster calculations, the electrons of the C, H and N atoms are described by triple- ξ basis set and of Fe by double- ξ plus polarization (DZVP2).⁵⁷ Electronic exchange and correlation effects were described within the generalized gradient approximation (GGA) in the Perdew–Burke–Ernzerhof (PBE) parametrization.^{58,59} No symmetry constraints were imposed. In deMon2k code, for all atoms, automatically generated auxiliary functions up to orbital quantum number, $l = 3$ were used for fitting the density with the GGA functionals.⁶⁰ The GGA functionals were also coupled to an empirical dispersion (D) term.⁶¹ A quasi-Newton method in internal redundant coordinates with analytical energy gradients was used for structure optimization of ferrous and ferric models with total spin $S=2$ and $S=5/2$, respectively. For the numerical integrations of the XC energy and potential, we used an adaptive grid with tighten threshold (10^{-8} a.u.).⁶² The convergence was based on the Cartesian gradient and displacement vectors with thresholds of 10^{-3} a.u. and the energy convergence was set to 10^{-7} a.u. The spin charge densities are computed using Mulliken

population scheme. The DFT calculations with periodic boundary conditions, carried out with VASP code, used the models 2e and 2a to build the unit cells for periodic calculations. In the case of the cluster model 1e, the corresponding periodic structure 2e was modelled using a cell size $17.19 \text{ \AA} \times 20.89 \text{ \AA}$. In the case of model 1a, the corresponding periodic structure 2a was constructed using cell size of $9.94 \text{ \AA} \times 12.64 \text{ \AA}$. Vacuum region of 15 \AA was introduced in the z -direction in order to eliminate interactions between the graphene sheet and its periodic images. All the DFT calculations with periodic boundary conditions (PBC) were performed using PBE exchange-correlation functional and VASP 5.2 recommended projector augmented-wave pseudopotentials.^{63,64} For the calculation of structural and electronic properties, standard PAW potentials supplied with VASP were used, with 4 valence electrons for C ($2s^2 2p^2$), with 5 electrons for O ($2s 2p^3$), 8 valence electrons for Fe ($4s^2 3d^6$), and 6 valence electrons for O ($2s 2p 4$), respectively. Electric field gradients at the positions of the Fe nuclei were calculated using the method reported in reference⁶⁵ as implemented in VASP. When calculating electric field gradient, we have used the corresponding GW potentials, which give a better description of high-energy unoccupied states. For GW Fe pseudopotential that treats 3s and 3p states as valence states was used. Cut-off energy for the plane wave basis set of 800 eV, break condition for electronic SC-loop of 10^{-6} eV and $8 \times 8 \times 1$ gamma centred mesh for the model 2a, and $4 \times 4 \times 1$ mesh for the model 2e were found to lead to the converged electric field gradients. In all cases, the Fermi-Dirac smearing method with sigma set to 0.03 was used. In addition, all the calculations included support grid for the evaluation of the augmentation charges. The Bader charge density analysis⁶⁶ with the implementation of Henkelman and co-workers⁶⁷ in VASP code was used to obtain the spin charge density of the periodic structures. The charge-spin density of the cluster structures was obtained using Mulliken population scheme.

The atomic spin densities were computed for all cluster and periodic models in order to verify the spin density at the ferric or ferrous Fe site. The Fe spin density in its high and intermediate spins was found to amount to $\sim 4e^-$ and $\sim 2e^-$, respectively.

High spin ferrous and ferric Fe models necessitated to increase the total spin of each system up to the spin density on Fe became $\sim 4e^-$. For comparison the Fe spin density in the intermediate spin state is $\sim 2e^-$. This is because important spin polarization at carbon or nitrogen happens, depending on the particular model size.

The quadrupole splitting energy is computed as the coupling between the nuclear quadrupole moment (Q) the non-spherical nucleus and the principle components V_{ii} ($i=x,y,z$) of the electric field gradient (EDF) tensor at ^{57}Fe nucleus using the following equation:

$$\Delta E_Q = \frac{1}{2} eQV_{zz} \sqrt{1 + \frac{\eta^2}{3}}$$

Where e is the charge of the electron and the asymmetry parameter η is computed as $\eta = (V_{xx} - V_{yy})/V_{zz}$, where $|V_{zz}| \geq |V_{yy}| \geq |V_{xx}|$. The nuclear quadrupole moment, Q , for $J=3/2$ state is taken to be 0.16 barn. Computation of ΔE_Q and η therefore becomes a question of computing the EFG tensor, which is readily obtained as an expectation value of the EFG operator, $V_{ij} = \langle \Psi_0 | \frac{3ij-r^2}{r^5} | \Psi_0 \rangle$, for the electronic ground state Ψ_0 and $i,j=x,y,z$ being the components of the electron radius vector r . For a direct comparison to experimentally reported values, calculated values of ΔE_Q are reported in units of $\text{mm}\cdot\text{s}^{-1}$.

References for Methods:

51. Ablett, J. M., Prieur, D., Céolin, D., Lassalle-Kaiser, B., Lebert, B., Sauvage, M., Moreno, T., Bac, S., Balédent, V., Ovono, A., Morand, M., Gélébart, F., Shukla, A. & Rueff, J. P. The GALAXIES inelastic hard X-ray scattering end-station at Synchrotron SOLEIL. *J. Synchrotron Radiat.* **26**, 263-271 (2019).
52. Rueff, J. P., Ablett, J. M., Ceolin, D., Prieur, D., Moreno, T., Balédent, V., Lassalle-Kaiser, B., Rault, J. E., Simon, M. & Shukla, A. The GALAXIES beamline at the SOLEIL synchrotron: inelastic X-ray scattering and photoelectron spectroscopy in the hard X-ray range. *J. Synchrotron Radiat.* **22**, 175-179 (2015).

53. de la Lande, A., Alvarez-Ibarra, A., Hasnaoui, K., Cailliez, F., Wu, X., Mineva, T., Cuny, J., Calaminici, P., López-Sosa, L., Geudtner, G., Navizet, I., Iriepa, C. G., Salahub, D. R.D. & Köster, A. M. Molecular Simulations with in-deMon2k QM/MM, a Tutorial-Review. *Molecules* **24**, 1653 (2019).
54. Koster, A. M. *et al.* *deMon2k*, Version 6, The deMon developers, Cinvestav, Mexico City (2018).
55. Kresse, G. & Furthmüller, J. Efficient iterative schemes for ab initio total-energy calculations using a plane-wave basis set. *Phys. Rev. B* **54**, 11169–11186 (1996).
56. Kresse, G. & Furthmüller, J. Efficiency of ab-initio total energy calculations for metals and semiconductors using a plane-wave basis set. *Comput. Mater. Sci.* **6**, 15–50 (1996).
57. Godbout, N., Salahub, D. R., Andzelm, J. & Wimmer, E. Optimization of Gaussian-type basis sets for local spin density functional calculations. Part I. Boron through neon, optimization technique and validation. *CJC Univ. Calg. 50th Anniv. Virtual Issue* **01**, 560–571 (2011).
58. Perdew, J. P., Burke, K. & Ernzerhof, M. Generalized Gradient Approximation Made Simple. *Phys. Rev. Lett.* **77**, 3865–3868 (1996).
59. Zhang, Y. & Yang, W. Comment on "Generalized Gradient Approximation Made Simple". *Phys. Rev. Lett.* **80**, 890–890 (1998).
60. Köster, A. M., Reveles, J. U. & Del, J. C. Calculation of exchange-correlation potentials with auxiliary function densities. *J. Chem. Phys.* **121**, 3417–3424 (2004).
61. Wu, Q. & Yang, W. Empirical correction to density functional theory for van der Waals interactions. *J. Chem. Phys.* **116**, 515–524 (2001).
62. Krack, M. & Köster, A. M. An adaptive numerical integrator for molecular integrals. *J. Chem. Phys.* **108**, 3226–3234 (1998).
63. Blöchl, P. E. Projector augmented-wave method. *Phys. Rev. B* **50**, 17953–17979 (1994).
64. Kresse, G. & Joubert, D. From ultrasoft pseudopotentials to the projector augmented-wave method. *Phys. Rev. B* **59**, 1758–1775 (1999).
65. Varret, F. Mössbauer spectra of paramagnetic powders under applied field: Fe²⁺ in fluosilicates. *J. Phys. Chem. Solids* **37**, 265–271 (1976).
66. Bader, R. F. W. *Atoms in Molecules: A Quantum Theory*. Oxford University Press. (1994).
67. Tang, W., Sanville, E. & Henkelman, G. A grid-based Bader analysis algorithm without lattice bias. *J. Phys. Condens. Matter* **21**, 084204 (2009).